Research Square

Preprints are preliminary reports that have not undergone peer review.
They should not be considered conclusive, used to inform clinical practice,
or referenced by the media as validated information.

Origin of Reduced Coercive Field in ScAlN: Synergy of Structural Softening and Dynamic Atomic Correlations

Ryotaro Sahashi
The University of Tokyo
Po-Yen Chen
The University of Tokyo
Teruyasu Mizoguchi
teru@iis.u-tokyo.ac.jp

The University of Tokyo

Article

Keywords:

Posted Date: June 1st, 2026

DOI: https://doi.org/10.21203/rs.3.rs-9699927/v1

License: This work is licensed under a Creative Commons Attribution 4.0 International License.
Read Full License

Additional Declarations: No competing interests reported.

Origin of Reduced Coercive Field in ScAlN: Synergy of Structural Softening and Dynamic Atomic Correlations

[1]Ryotaro Sahashi, [1]Po-Yen Chen, and [1,2]Teruyasu Mizoguchi (corresponding author)
Email: teru@iis.u-tokyo.ac.jp
[1]Department of Materials Engineering, The University of Tokyo, Tokyo, Japan
[2]Institute of Industrial Science, The University of Tokyo, Tokyo, Japan

Abstract
Among wurtzite-type ferroelectrics, scandium-doped aluminum nitride (ScAlN) has emerged as a leading candidate for CMOS-compatible low-voltage memory, combining strong spontaneous polarization with process compatibility. A remarkable feature of this system is the pronounced reduction of the coercive field (E_c) with increasing Sc concentration; however, its microscopic origin remains poorly understood at the atomic scale, particularly under finite temperature and applied electric fields. Here, we integrate a density-functional-theory–accurate machine-learning force field with an equivariant neural-network–based Born effective charge model to perform large-scale electric-field-driven molecular dynamics simulations at near-first-principles accuracy. The framework correctly reproduces the experimentally observed qualitative trends in key experimental trends, including the decrease in the c/a ratio and the monotonic reduction of E_c with increasing Sc content. Beyond static structural softening, we uncover a dynamic mechanism underlying E_c reduction. Sc atoms exhibit larger thermal vibrations and undergo preceding displacements during switching, acting as dynamic triggers for polarization reversal. Moreover, the displacement correlation between Sc and Al atoms evolves systematically with composition, enhancing cooperative atomic rearrangements and lowering the effective switching barrier. These results demonstrate that E_c reduction in ScAlN arises from the synergy of structural softening and dynamic correlation evolution, providing a new perspective for designing hexagonal ferroelectrics.

1. Introduction
Ferroelectric random-access memory (FeRAM) has attracted considerable attention as a key device for realizing in-memory computing (IMC) in emerging artificial intelligence (AI) hardware, owing to its ability to achieve both fast write speeds and low power consumption.[1–3] Among candidate materials, scandium-doped aluminum nitride (ScAlN) has garnered strong interest from both industry and academia because, unlike conventional perovskite oxides, it combines excellent ferroelectric properties with high compatibility with CMOS fabrication processes.[4–8]

A particularly notable feature of ScAlN is the dramatic reduction of the coercive field (E_c) with increasing Sc concentration, which opens the path toward low-voltage device operation.[9–11] Nevertheless, the E_c values remain substantial, probing a critical bottleneck for practical low-voltage operations in logic-in-memory architectures. While the macroscopic reduction of E_c is well-established, the lack of a comprehensive understanding of the underlying atomistic switching dynamics hinders the rational design of next-generation ferroelectrics with further optimized performance. To date, the mechanism of E_c reduction has been primarily discussed based on static energy analyses using first-principles density functional theory (DFT) calculations.[12] Previous studies have pointed out that the incorporation of Sc relaxes the structural anisotropy of the crystal lattice and reduces the energy difference between the polar wurtzite phase and the nonpolar hexagonal phase. This so-called “structural softening” lowers the polarization reversal barrier on the static potential energy surface (PES).[13]

In contrast, actual ferroelectric switching is an inherently dynamic process that proceeds under finite temperature and applied electric fields. Static PES analyses alone are insufficient to fully capture the dynamic picture, such as how atoms overcome the energy barrier through thermal fluctuations or how Al and Sc atoms cooperate via distinct roles and correlated responses during polarization reversal. To address these dynamic aspects, ab initio molecular dynamics (AIMD) based on DFT has been widely employed to investigate electric-field-induced structural changes.[14,15] However, due to its extremely high computational cost, AIMD is restricted to limited spatial and temporal scales, making it difficult to achieve the statistical accuracy required to discuss composition dependence and correlated atomic motions in solid-solution systems.

To overcome these limitations, computational approaches based on empirical simulations and machine-learning force fields (MLFFs) have increasingly been applied in materials science in recent years.[16–19] In particular, MLFFs have advanced rapidly through the development of graph neural network–based frameworks such as MACE, ORB, and SevenNet,[20–22] as well as descriptor-based approaches such as GRACE. Indeed, MLFF-based molecular dynamics (MD) simulations have been shown to accurately reproduce structural and dynamical properties consistent with first-principles calculations across a wide range of environments—including crystalline, liquid, and amorphous phases—in prototypical ferroelectrics such as $BaTiO_3$, thereby demonstrating their reliability for large-scale and long-time MD simulations.[23] MLFFs are data-driven models trained on high-accuracy first-principles datasets, enabling the prediction of interatomic forces and energies with near-DFT accuracy. Furthermore, approaches that integrate ML potentials with Born effective charge (BEC) prediction models have been successfully applied to representative ferroelectrics such as $BaTiO_3$ and HfO_2.[24,25] Nevertheless, these studies have been largely limited to perovskite or fluorite structures, and applications to wurtzite-structured ScAlN that prove its switching mechanism in depth remain scarce.

In this study, we aim to physically elucidate the origin of the reduced E_c in ScAlN by integratively analyzing both "static structural softening" and "dynamic atomic dynamics." To this end, we construct a MLFF based on MACE,[26] which retains DFT-level accuracy while enabling large-scale and long-time simulations, and integrate it with an equivariant neural network–based BEC prediction model.[27] This framework allows us to atomistically track large-scale switching processes under applied electric fields that are inaccessible to conventional static calculations or AIMD approaches. [24,25] We demonstrate that, in addition to the static lattice destabilization induced by increasing Sc concentration, the evolution of correlated atomic displacement responses among cations—triggered by the large-amplitude thermal fluctuations of Sc atoms—can play a crucial role in polarization reversal.

2. Results and Discussion

To perform MD simulations under an applied electric field, interatomic forces predicted by the fine-tuned MACE model were combined with electric-field-induced forces derived from BECs predicted by the fine-tuned BM1 model.

The external electric-field-induced force acting on atom i, denoted as F_{ext}, was calculated at each MD step following the method proposed by Chen et al.[24,25] according to **Equation (1):**

$$F_{\text{ext}} = | e | \mathcal{E}_\beta Z^*_{i,\beta\alpha} \quad (1)$$

In Equation (1), e is the elementary charge, $\mathcal{E}_\beta$ is the applied electric-field vector, and $Z^*_{i,\beta\alpha}$ is the BEC tensor predicted by the equivar_eval model.

The total force acting on each atom during time integration was given as the sum of the interatomic force calculated by MACE and the external electric-field-induced force defined above.

All electric-field-coupled MD simulations were performed under the NPT ensemble. The applied electric field was swept cyclically following:

$$0 \rightarrow -20 \rightarrow +20 \rightarrow 0 \text{ MV cm}^{-1}.$$

Prior to the main analysis, we systematically validated both the MLFF models and the simulation setup to ensure quantitative reliability (see Supporting Information S1 and S2 for full details). All validation tests were conducted using a representative composition, $Sc_{0.25}Al_{0.75}N$.

Regarding model accuracy, fine-tuning of the MACE-MP-0 foundation model[26] on the ScAlN-specific PBE dataset dramatically improved the prediction errors to 0.22 meV/atom for energies and 6.4 meV/Å for atomic forces on the held-out test set, outperforming all other state-of-the-art universal MLFFs benchmarked in this study (Figure S1, Table S1). The BEC prediction model (BM1)[27] similarly achieved mean absolute errors of 0.020 e, 0.011 e, and 0.014 e for Sc, Al, and N atoms, respectively, after fine-tuning, confirming first-principles-level accuracy in the electric-field-induced forces applied during MD (Figure S3).

For the simulation setup, we verified that including long-range Coulomb interactions (short-range vs. long-range[28]) produces negligibly different polarization-electric field (P–E) hysteresis loops and E_c and accordingly adopted the computationally efficient short-range model (Figure S4(a)). Supercell-size convergence was confirmed by comparing 360-atom and 2880-atom supercells, which yielded E_c values of 9.33 and 8.82 MV cm^{-1}, respectively, a difference of less than 6% (Figure S4(b)). Finally, we confirmed that switching from a stepwise to a continuous electric-field ramp protocol does not significantly alter the ferroelectric characteristics, validating the continuous ramp approach adopted for the dynamic analyses presented below (Figure S4(c)). A real-time visualization of the atomic evolution during this continuous electric-field-driven polarization switching is provided in **Movie S1**.

These validations collectively confirm that the present simulation framework is both accurate and well-converged, providing a reliable basis for the quantitative analyses that follow. Having established this foundation, we now examine the dynamic switching behavior of ScAlN, beginning with the sweep-rate dependence of the E_c. As detailed in Section S2.4, evaluating the dynamic response under varying sweep rates revealed that E_c converges near the quasi-static limit at 0.05 kV cm^{-1} fs^{-1} (**Figure S5**). Because this rate optimally balances physical fidelity with computational cost, it was adopted for all subsequent simulations in this study.

2.1. Ferroelectric Switching Behavior and Composition Dependence

We now turn to the intrinsic ferroelectric switching behavior of $Sc_xAl_{1-x}N$ and its composition dependence. All simulations presented hereafter were performed using a 360-atom supercell with the Short-Range model under a continuous electric-field ramp of 0.05 kV cm^{-1} fs^{-1}.

The monotonic reduction of E_c with increasing Sc concentration is among the most reproducible and technologically significant features of ScAlN ferroelectrics, consistently reported across independent experimental studies.[11,29,30] While structural softening and extrinsic effects such as nitrogen vacancies and Sc clustering have been proposed as contributing factors, disentangling their respective roles experimentally is extremely challenging, as film deposition inevitably introduces defects and compositional inhomogeneities that obscure intrinsic switching behavior. Atomistic simulations free from such extrinsic perturbations thus provide a unique opportunity to isolate the intrinsic mechanism. We first examine how the macroscopic P–E characteristics evolve with Sc concentration, and then identify the microscopic atomistic origin of the observed E_c reduction.

Figure 1(a) shows the calculated P–E hysteresis loops for each Sc composition. As the Sc concentration increases,

systematic changes are observed in both the polarization switching characteristics and the overall hysteresis shape. To confirm the microscopic origin of the polarization reversal, atomic configurations at the maximum positive and negative electric fields were analyzed. As shown in Figure 1(b) and 1(c), the structures at the maximum positive field correspond to the M-polar configuration, while those at the maximum negative field correspond to the N-polar configuration. Inspection of the atomic displacements clearly confirms the formation of the two opposite polar states in the wurtzite lattice, demonstrating that the present framework correctly reproduces polarization switching between M-polar and N-polar structures.

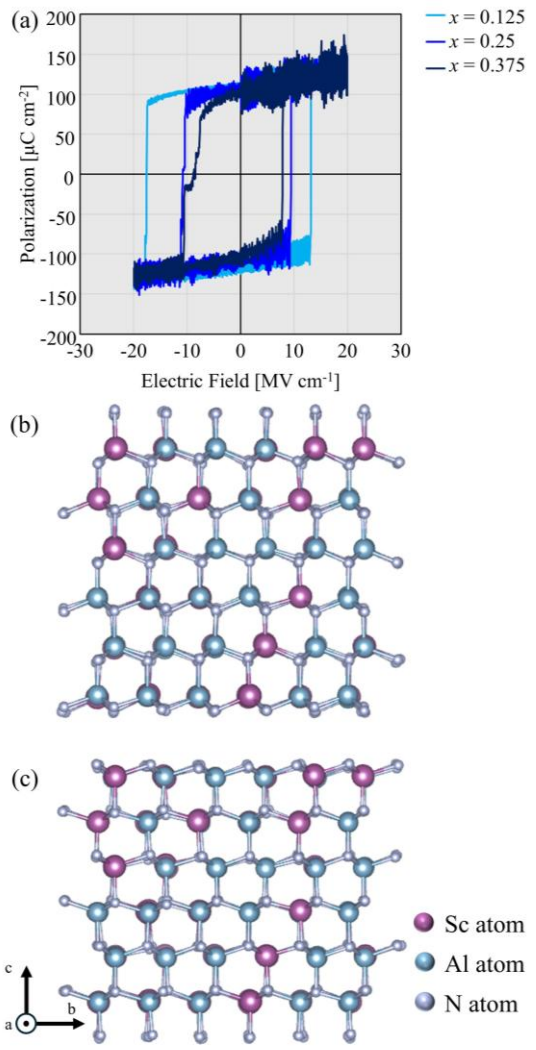


Figure 1. Dependence on Sc concentration. (a) *P–E* hysteresis loops for Sc concentrations of $x = 0.125$ (light blue), 0.25 (blue), and 0.375 (navy). (b) M-polar structure at the positive maximum electric field and (c) N-polar structure at the negative maximum electric field. Structures in panels (b) and (c) are taken from simulations using the $x = 0.25$.

The present calculations reproduce the monotonic reduction of E_c with increasing Sc concentration over the entire composition range, in good qualitative agreement with multiple experimental reports (Ref. [11,29–33]). In particular, the experimentally observed high-field reduction trend of E_c is consistently captured by the simulations

The quantitative composition dependence of E_c is further examined in **Figure 2**. Experimentally reported E_c values exhibit substantial scatter across studies, reflecting the strong sensitivity of ferroelectric switching to extrinsic factors, particularly nitrogen vacancy concentration, deposition atmosphere, and local Sc clustering. Films grown under a pure N_2 atmosphere, which suppresses vacancy formation and most closely approximates intrinsic switching conditions, yield systematically higher E_c than those deposited under Ar+N_2 atmospheres (Ref. [11,30–33]).

The present calculations systematically exceed the majority of experimental E_c values, which is physically consistent with the defect-free nature of the SQS simulation model. Among the datasets in Figure 2(a), the pure N_2-deposited films of Ref.[29], representing the most intrinsic experimental conditions, show the closest agreement, supporting the interpretation that the calculations capture the upper bound of E_c. The monotonic reduction trend with increasing Sc concentration is robustly reproduced across the entire composition range.

The calculated P_r shows a weaker composition dependence than experimental reports, which is consistent with the slight overestimation of the c/a ratio seen in Figure S2(a). The slight overestimation of the c/a ratio, a known tendency of PBE-based calculations for nitride systems, leads to a moderated reduction in spontaneous polarization with increasing Sc content.

Nevertheless, the primary objective of this study is to elucidate the atomistic origin of

E_c reduction, for which correct reproduction of the monotonic decreasing trend is the essential criterion. The present framework satisfies this criterion and provides a physically consistent basis for the mechanistic analysis that follows.

2.2. Atomistic origins: Sc-triggered switching and evolution of interatomic correlations

Having established the quantitative reliability of the simulation framework and confirmed the correct reproduction of the composition-dependent E_c reduction, we now turn to its atomic-level origin. The central question is why increasing Sc concentration so systematically lowers the switching barrier, a question that static energy analyses alone cannot fully resolve. In the following sections, we address this from two complementary perspectives. We first examine the static structural distortion induced by Sc incorporation, and then analyze the dynamic evolution of interatomic displacement correlations directly extracted from electric-field-driven MD simulations.

2.2.1. Structural softening driven by internal structural parameters

Figure 2(b) shows the internal structural parameters of Al and Sc for $Sc_xAl_{1-x}N$ at compositions of x = 0.125, 0.25, and 0.375. The structural distortion of the wurtzite lattice is characterized by the internal structural parameter u, which describes the relative displacement between the cation and anion sublattices along the c-axis. In wurtzite-type ferroelectrics, this parameter directly reflects the atomic configuration relevant to polarization switching, because polarization reversal occurs primarily through atomic displacements along the c-axis. The parameter is defined as shown in **Equation (2):**

$$u = \frac{z_N - z_{cation}}{c} \qquad (2)$$

In Equation (2), z_N and z_{cation} denote the fractional coordinates of the nitrogen atom and the nearest cation (Al or Sc), respectively, and c is the lattice constant along the polarization direction.

Figure 2(b) summarizes the composition dependence of u for Al and Sc atoms. For all compositions studied, Al atoms exhibit values close to the ideal wurtzite parameter u = 0.375, whereas Sc atoms systematically

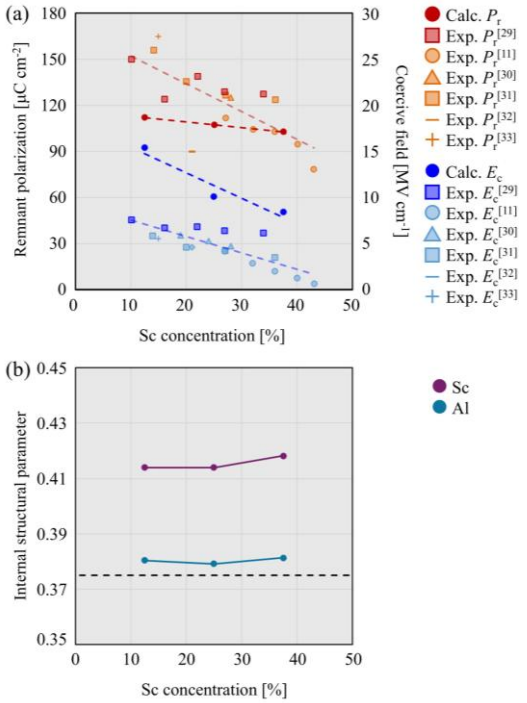


Figure 2. (a) Composition dependence of the P_r (left axis) and E_c (right axis) as a function of Sc concentration. Circles represent the calculated values obtained in this study, while squares indicate experimental data reported in Ref. [11,29–33]. (b) Composition dependence of the internal structural parameter u. Values for Sc atoms are shown in purple and those for Al atoms in light blue. The black dashed line indicates the ideal internal parameter value of u = 0.375 for the wurtzite structure.

show larger deviations from the ideal value. This indicates that the local bonding environment around Sc atoms is inherently more distorted and closer to configuration favorable for polarization reversal.

From a macroscopic perspective, increasing the Sc concentration increases the fraction of locally distorted environments characterized by larger u values. Such deviations from ideal tetrahedral coordination reduce structural anisotropy and weaken the restoring forces opposing polarization reversal. This composition-induced lattice softening is consistent with the experimentally observed decrease in the

c/a ratio and has been previously interpreted as a reduction of the static switching barrier on the potential energy surface.

Therefore, static structural softening clearly contributes to the reduction of E_c with increasing Sc concentration. However, the magnitude of the E_c decrease and its systematic nature raise the question of whether static lattice distortion alone is sufficient to account for the observed trend. Because polarization switching occurs under finite temperature and electric field, dynamic atomic motion and cooperative displacement responses may play an additional role beyond the static structural picture.

To address this possibility, we next examine the atomic-scale switching dynamics directly extracted from electric-field-driven MD simulations.

2.2.2 Dynamic Triggering by Sc Atoms

While static structural softening provides an important contribution, ferroelectric switching is fundamentally a dynamic process under finite temperature and applied electric field. A key question is whether all atomic species respond simultaneously to the applied field, or whether specific atoms initiate the switching event, and if so, whether this sequential response directly lowers the macroscopic switching barrier. To address this, we analyze the time- and field-dependent atomic displacements obtained from electric-field-driven MD simulations.

Figure 3 shows the relationship between the applied electric field and the atomic displacements along the polarization direction (Δz) for Sc, Al, and N atoms at Sc concentrations of x = 0.125, 0.25, and 0.375. To quantitatively compare the onset of switching among different atomic species, we define an atomic coercive field $E_{c,atom}$ as the electric field at which the displacement of a given atomic species changes sign relative to the centrosymmetric reference configuration.

Because atomic trajectories at finite temperature contain thermal fluctuations, a moving-average smoothing procedure was applied to the displacement–field curves to accurately determine the zero-crossing point. The resulting $E_{c,atom}$ are summarized in **Table 1**.

Table 1. $E_{c,atom}$, atom evaluated for each atomic species. Values are derived from the atomic displacement–electric field data shown in Figure 3.

Sc ntration	$E_{c,Sc}$ / MV cm^{-1}	$E_{c,Al}$ / MV cm^{-1}	$E_{c,N}$ / MV cm^{-1}
= 0.125	13.07	13.19	13.18
= 0.25	10.09	10.36	10.36
= 0.375	7.72	7.84	7.82

Across all compositions examined, Sc atoms consistently exhibit slightly lower $E_{c,atom}$ than Al atoms. For example, at x = 0.25, $E_{c,Sc}$ = 10.09 MV cm^{-1}, whereas $E_{c,Al}$ = 10.36 MV cm^{-1}. Similar differences are observed at other compositions. This result quantitatively demonstrates that Sc atoms initiate displacement reversal earlier than Al atoms under the applied electric field. Their differences are small in absolute magnitude (0.12~0.27MV cm^{-1}) but are reproduced consistently across all three compositions and other SQS configurations, suggesting a systematic rather than statistical origin. This trend is consistent with Sc atoms initiating displacement reversal marginally earlier than Al atoms under the applied field.

In addition to the earlier onset of displacement, Sc atoms exhibit larger thermal vibration amplitudes compared to Al atoms, as evidenced by the broader spread of Δz in Figure 3. This vibrational hierarchy (Al < Sc) indicates that Sc atoms experience a shallower local potential and are more susceptible to field-induced displacement. Together, the earlier displacement onset and enhanced vibrational amplitude are consistent with Sc atoms acting as dynamic triggers for polarization reversal, locally perturbing the lattice and facilitating collective atomic rearrangement.

Importantly, this triggering behavior cannot be inferred solely from static structural

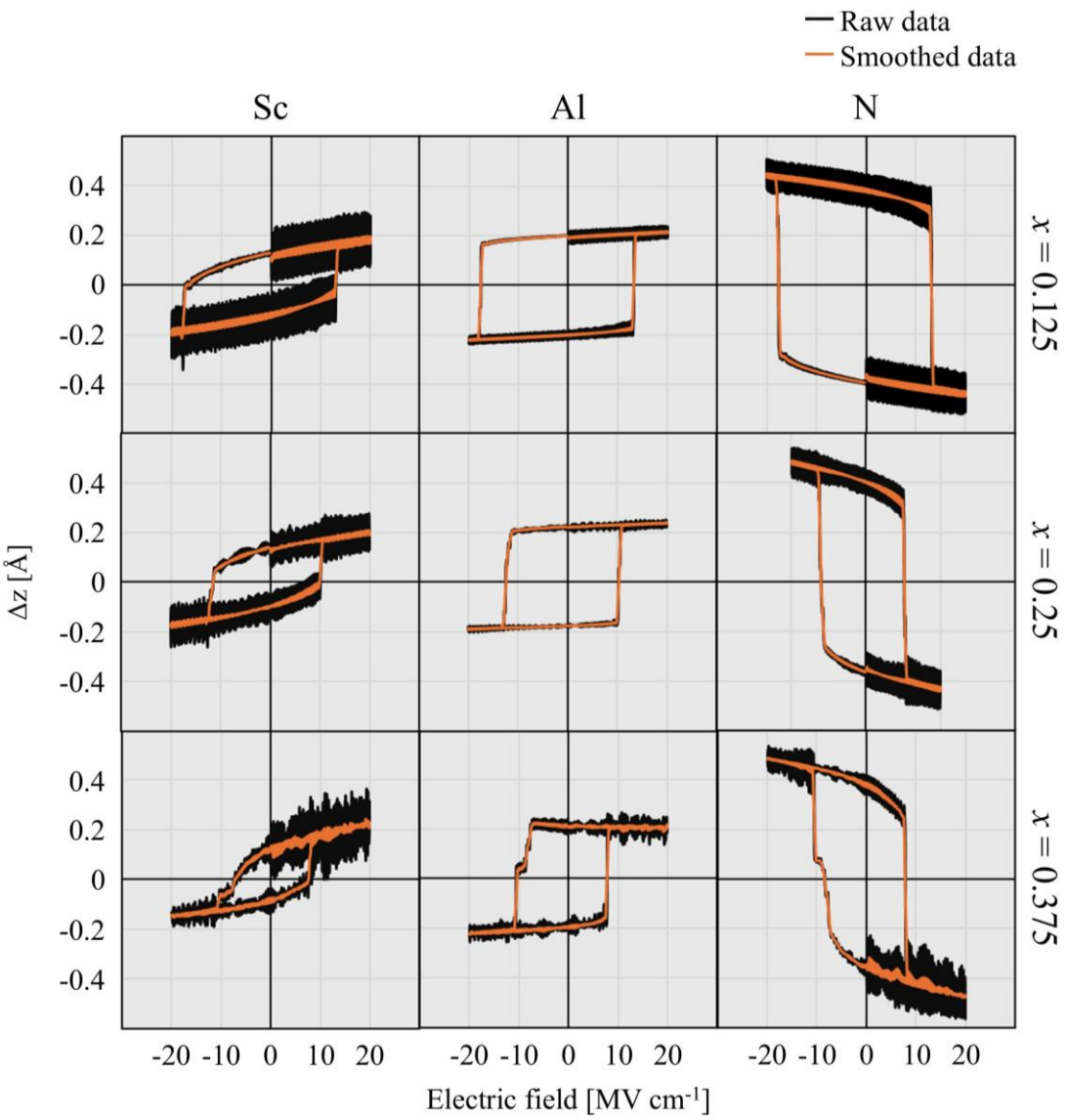


Figure 3. Relationship between applied electric field and z-direction atomic displacement Δz obtained from electric-field-driven MD simulations. Plots are arranged in a 3×3 matrix, with rows corresponding to Sc concentrations of x = 0.125, 0.25, and 0.375 from top to bottom. Columns represent Sc (left), Al (center), and N (right) atoms. Black curves represent the raw atomic displacement data obtained directly from the MD simulations, while orange curves indicate the data after smoothing using a moving average over five consecutive points.

parameters. While static distortion lowers the intrinsic energy barrier, the dynamic response reveals how individual atomic species contribute differently to the switching pathway. The earlier displacement of Sc atoms has a direct consequence for the macroscopic switching barrier. Because Sc atoms initiate reversal at a lower field, the remaining Al sublattice is already displaced into a partially switched configuration by the time the bulk switching event occurs. This effectively reduces the energy cost for the subsequent collective Al displacement, lowering the apparent *Ec*. The enhanced thermal amplitude of Sc atoms further amplifies this effect: larger vibrational excursions increase the probability that thermal fluctuations alone carry Sc atoms across the local potential barrier, allowing field-assisted switching to commence at a smaller applied field.

However, polarization reversal in a crystalline solid is inherently cooperative. The displacement of one atomic species must be accommodated by correlated motion of neighboring atoms. Therefore, to

fully understand how Sc incorporation reduces E_c, it is necessary to examine how these local dynamic perturbations propagate through the lattice via interatomic displacement correlations. This issue is addressed in the following section.

2.3. Evolution of Interatomic Displacement Correlations and Unified Mechanism

To understand how the local dynamic instability of Sc atoms propagates through the lattice and contributes to macroscopic switching behavior, we performed a correlation analysis of atomic displacements during electric-field-driven MD simulations.

Specifically, for each composition, we evaluated the linear correlation between the z-direction displacement of Sc atoms (Δz_{Sc}) and those of neighboring Al and N atoms per electric-field step. The resulting correlation slopes quantify both the strength and phase relationship of cooperative atomic response under the applied electric field.

Figure 4 shows the displacement correlations for different Sc concentrations. For all compositions, N atoms exhibit a negative correlation with Sc displacements, indicating a robust anti-phase response consistent with the alternating cation–anion displacement characteristic of polarization reversal. The slopes for N remain relatively stable across compositions, suggesting that the anion framework plays a structurally constraining role during switching.

In contrast, the behavior of Al atoms evolves systematically with increasing Sc concentration. At low Sc concentration (x = 0.125), Al displacements are positively correlated with Sc displacements, indicating in-phase cooperative motion. As the Sc content increases, the magnitude of this positive slope decreases. At higher Sc concentration (x = 0.375), the slope becomes negative, revealing a qualitative transition to partially out-of-phase motion between Al and Sc atoms.

This sign reversal of the Al–Sc displacement correlation represents a

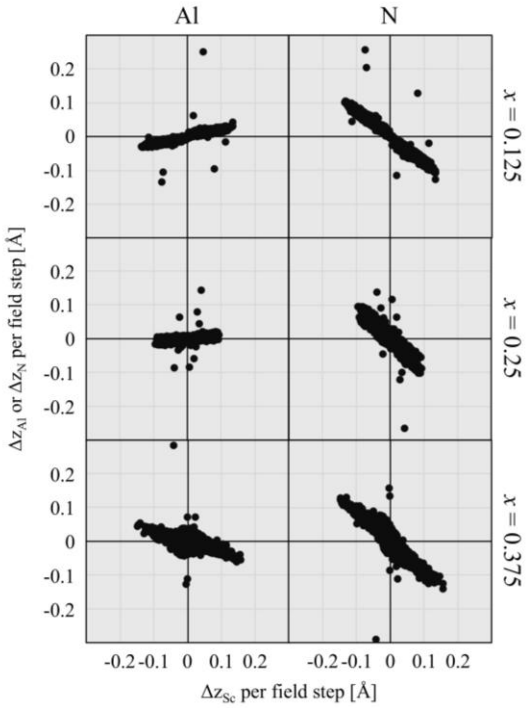


Figure 4. Correlation analysis of atomic displacements. Correlations between Sc atomic displacement per electric-field step and z-direction displacements of Al atoms (left column) and N atoms (right column). Plots are arranged in a 3×2 matrix, with rows corresponding to Sc concentrations of x = 0.125, 0.25, and 0.375 from top to bottom.

fundamental change in cooperative response mode, and its physical origin can be traced to the difference in bond strength between Sc-N and Al-N pairs. Crystal orbital Hamilton population (COHP) analysis yields average -ICOHP values of around 3.0 eV for Sc-N bonds and 4.7 eV for Al-N bonds, demonstrating that Sc-N bonds are weaker. This bond-strength hierarchy directly determines the local potential experienced by each cation species: Sc atoms occupy a shallower potential well, which accounts for both their larger thermal vibration amplitudes and their earlier onset of field-driven displacement established in Section 2.2.2.

As Sc concentration increases, the fraction of weaker Sc-N bonds in the lattice grows, progressively altering the mechanical coupling between cation sublattices. At low Sc concentration, the rigid Al-N network dominates, constraining Sc displacements into synchronized, in-phase motion with Al.

At higher Sc concentration, the increasing prevalence of compliant Sc-N bonds weakens this constraint: Sc atoms can undergo larger displacements relative to Al without transmitting proportional restoring forces back through the lattice.

This mechanical decoupling gives rise to the observed transition from in-phase to partially out-of-phase Al-Sc correlation. Critically, this partially decoupled response enables a sequential switching pathway: Sc atoms, driven by their weaker bonding environment, initiate displacement reversal first, lowering the local energy landscape for the subsequent Al displacement. This sequential process carries a lower cooperative energy cost than the fully concerted switching required at low Sc concentration, directly contributing to the reduction of macroscopic E_c.

The evolution of displacement correlation directly parallels the monotonic reduction of E_c observed in Figure 2(a). The quantitative correspondence between the sign change of the Al-Sc correlation slope and the composition-dependent E_c reduction strongly suggests that this reorganization of cooperative displacement modes is a governing factor in the switching barrier, operating in addition to static structural softening.

Taken together, the results reveal a unified mechanism for E_c reduction in ScAlN. Static structural softening, characterized by deviation of the internal parameter u, lowers the intrinsic polarization-reversal barrier. Simultaneously, dynamic correlation evolution modifies how atomic displacements propagate through the lattice under finite temperature and electric field. The synergy between these static and dynamic effects reduces the effective switching barrier and gives rise to the pronounced composition-dependent decrease in E_c.

Importantly, this mechanism extends beyond a purely energetic description on a static potential energy surface. Instead, it highlights the essential role of dynamic correlation engineering—the systematic modification of cooperative atomic displacement patterns—as a governing factor in ferroelectric switching.

This dynamic perspective provides a concrete design criterion for hexagonal ferroelectrics that goes beyond the conventional static-barrier picture: an effective dopant must simultaneously satisfy two conditions. First, it must locally soften the host lattice by deviating the internal structural parameter u toward the transition-state configuration (structural softening condition). Second, its displacement correlation with the host cation must transition toward anti-phase response within the experimentally accessible composition range (dynamic correlation condition). Candidate dopants can be screened against these two criteria using the simulation framework established here, offering a computationally efficient route to identify substituents that optimize the trade-off between switching field and polarization in hexagonal ferroelectrics.

3. Conclusion

In this study, we established a first-principles-accurate simulation framework for wurtzite ferroelectric $Sc_xAl_{1-x}N$ by integrating a fine-tuned MLFF with an equivariant neural-network-based Born effective charge model. This approach enabled large-scale electric-field-driven MD simulations capable of quantitatively reproducing experimentally observed trends in lattice anisotropy and E_c reduction. We demonstrated that the E_c decreases monotonically with increasing Sc concentration and clarified its microscopic origin from both static and dynamic perspectives. Static structural softening, characterized by systematic deviation of the internal structural parameter u, lowers the intrinsic polarization-reversal barrier. Beyond this static picture, we revealed that Sc incorporation induces a qualitative evolution of cation-cation displacement correlations during switching. This evolution is rooted in the weaker Sc-N bonding relative to Al-N, as quantified by COHP analysis (-ICOHP: ~3.2 eV vs. ~4.8 eV), which places Sc atoms in a shallower

local potential and renders them more susceptible to field-driven displacement. Sc atoms exhibit enhanced thermal instability and initiate displacement reversal earlier than Al atoms, while the correlation between Sc and Al displacements transitions from predominantly in-phase to partially out-of-phase motion with increasing Sc concentration. This mechanical decoupling enables a sequential switching pathway in which Sc atoms initiate reversal first, reducing the cooperative energy cost for the subsequent Al displacement and lowering the effective switching barrier under applied electric field.

These results demonstrate that E_c reduction in ScAlN cannot be understood solely within a static potential-energy framework. Instead, it arises from the synergy between structural softening and dynamic correlation evolution, the latter being driven by the composition-dependent reorganization of mechanical coupling between cation sublattices. The concept highlighted in this work—engineering cooperative atomic response modes to lower switching barriers—provides a dynamic design principle for hexagonal ferroelectrics and offers guidance for developing low-voltage ferroelectric materials.

4. Methods

4.1. Construction of the ScAlN Database

To fine-tune a MACE model specialized for the ScAlN system, we employed a first-principles dataset publicly available from Ref. [34].

The reference calculations were performed using the Vienna Ab initio Simulation Package (VASP)[35–38] based on the projector augmented-wave (PAW) method.[39] The dataset consists of 256-atom supercell structures of $Sc_xAl_{1-x}N$ calculated using the PBE exchange‐correlation functional,[40] with four Sc compositions: x = 0, 0.125, 0.25, and 0.375.

The dataset contains a total of 1664 structures. To rigorously evaluate the generalization performance of the model, the dataset was randomly divided into a training set (1332 structures) and a test set (332 structures). The predictive accuracy on the test set, which was not used during training, was used to assess the reliability of the model.

In the reference calculations, the PBE exchange–correlation functional was employed, and Brillouin-zone integration was restricted to the Gamma point (1×1×1). From this public dataset, the total energies, atomic forces, and stress tensors were extracted and used for training the MLFF. To investigate the bond strength, ICOHP was calculated using Lobster code[41–43].

4.2. Development of the MACE Model

To improve the modeling accuracy for ScAlN, we fine-tuned the general-purpose MLFF MACE-MP-0[26] using the PBE-based dataset described in Section 4.1. MACE-MP-0 served as a foundation model, and the fine-tuning process enabled adaptation to the structural and energetic characteristics specific to ScAlN.

The dataset split followed the procedure described in Section 4.1. Training was performed using a batch size of 2 and an initial learning rate of 0.01 with the AMSGrad optimizer. During the early stage of training, an exponential moving average (EMA) of model weights was applied to stabilize convergence. After the validation loss reached a plateau, stochastic weight averaging (SWA) was introduced. Early stopping was applied when the validation loss failed to improve for five consecutive epochs.

The total loss, defined as an equally weighted sum of energy and atomic force errors, decreased consistently throughout the training process. As a result, a model with high predictive accuracy on the test dataset was obtained.

4.3. Born Effective Charge Calculation

Most existing MLFFs are trained solely on structural and energetic information and do not explicitly incorporate electronic properties. This limitation becomes critical for systems in which electric-field effects

play a central role. To quantitatively evaluate polarization changes induced by atomic displacements and to directly account for electric-field-induced forces, the introduction of BECs is essential.[44–46]

In this study, we adopted the equivar_eval model (architecture: BM1), an equivariant graph convolutional neural network developed by Kutana et al.[27]

The same structural dataset used for MACE training (Train: 1332, Test: 332) was employed for training and testing the BEC prediction model. Since the original public dataset does not provide reference BEC values, BECs were independently calculated in this study using density functional perturbation theory (DFPT). DFPT calculations were performed using the VASP code, employing the PBE functional and Gamma-point sampling to ensure consistency with the force-field training data, and were carried out for fully relaxed structures.

Fine-tuning of the BEC model was conducted using a batch size of 16, a learning rate of 5×10^{-3}, and the AdamW optimizer. Training continued for up to 300 epochs, with early stopping applied if no improvement was observed for 20 epochs. The loss function was defined as the L1 loss between predicted and DFPT reference BEC values. Through this procedure, a BEC prediction model with substantially reduced test-set error was obtained, providing sufficient accuracy for subsequent electric-field-driven MD simulations.

4.4. Polarization Evaluation and Construction of the *P–E* Hysteresis Loop

To evaluate the electric polarization under an external electric field and to construct *P–E* hysteresis loops, the polarization was calculated at each electric-field step during the electric-field-coupled MD simulations. The polarization P was evaluated using atomic displacements and born effective charges according to **Equation (3)**:

$$\boldsymbol{P} = \frac{\boldsymbol{e}}{\boldsymbol{V}} \sum_{\boldsymbol{i}} \boldsymbol{Z_i^*}\, \boldsymbol{\Delta z_i} \qquad (3)$$

In Equation (3), e is the elementary charge, V is the instantaneous cell volume, $\boldsymbol{Z_i^*}$ denotes the BEC of atom i predicted by the fine-tuned ML model, and $\boldsymbol{\Delta z_i}$ represents the displacement of atom i along the polarization direction relative to the centrosymmetric nonpolar reference structure.

As the reference structure for evaluating $\boldsymbol{\Delta z_i}$, we adopted a nonpolar configuration in which N lie on the same atomic plane (i.e., the same layer) as the cations (Al/Sc), as shown in Figure S2(b). This structure possesses inversion symmetry and corresponds to zero polarization. Atomic displacements relative to this reference structure were combined with the corresponding BEC values to compute the polarization using Equation (3).

At each electric-field step, the system was equilibrated for 20 ps, followed by a 10 ps sampling period during which atomic positions were recorded. Time-averaged atomic displacements were calculated from this trajectory, and the average polarization was obtained accordingly. The *P–E* hysteresis loop was constructed by plotting the averaged polarization as a function of the applied electric field.

This procedure ensures a consistent evaluation of polarization based on dynamically computed atomic displacements and fine-tuned BECs, enabling accurate and efficient modeling of ferroelectric switching behavior within the MLFF-based MD framework.

Acknowledgements

This study was supported by the Ministry of Education, Culture, Sports, Science and Technology (MEXT), and New Energy and Industrial Technology Development Organization (NEDO). P.-Y.C. would like to acknowledge the support of JST SPRING (Grant Number JPMJSP2108). The computation was carried out using the computer resource offered by Research Institute for Information Technology, Kyushu University.

Author Contributions

R.S. and P.-Y.C. conceived the idea and designed the research. R.S. performed the simulations, analyzed the data, and prepared the figures. R.S. wrote the original draft of the manuscript. T.M. supervised the project and acquired funding. All authors discussed the results, reviewed, and edited the manuscript.

Data Availability Statement

The trained machine-learning force field models, Born effective charge models, and simulation trajectories generated in this study are available from the corresponding author upon reasonable request.

References

1. **Wang, A., Chen, R., Yun, Y., Xu, J. & Zhang, J. Review of Ferroelectric Materials and Devices toward Ultralow Voltage Operation.** ***Adv. Funct. Mater.*** **35, (2025).**
2. **Guido, R.** ***et al.*** **Kinetics of N- to M-Polar Switching in Ferroelectric Al $_{1-x}$ Sc $_{x}$ N Capacitors.** ***Advanced Science*** **11, (2024).**
3. **Yang, Y.** ***et al.*** **Thickness-Driven Transition of Switching Kinetics in Wurtzite Ferroelectrics.** ***Adv. Funct. Mater.*** **36, (2026).**
4. **Wang, R.** ***et al.*** **Composition-Graded Nitride Ferroelectrics Based Multi-Level Non-Volatile Memory for Neuromorphic Computing.** ***Advanced Materials*** **37, (2025).**
5. **Yang, G.** ***et al.*** **Unveiling the Pockels coefficient of ferroelectric nitride ScAlN.** ***Nat. Commun.*** **15, 9538 (2024).**
6. **Yang, D.-P.** ***et al.*** **Emerging ferroelectric materials ScAlN: applications and prospects in memristors.** ***Mater. Horiz.*** **11, 2802–2819 (2024).**
7. **Liu, Y.** ***et al.*** **Polarization Switching on the Open Surfaces of the Wurtzite Ferroelectric Nitrides: Ferroelectric Subsystems and Electrochemical Reactivity.** ***Advanced Materials*** **38, (2026).**
8. **Nguyen, T.** ***et al.*** **Large Built-in Fields and Tunable Ferroelectricity in Composition-Graded ScAlN Thin Films Deposited by Reactive Sputtering.** ***Advanced Science*** **12, (2025).**
9. **Zhang, Y., Zhu, Q., Tian, B. & Duan, C. New-Generation Ferroelectric AlScN Materials.** ***Nanomicro Lett.*** **16, 227 (2024).**
10. **Uehara, M.** ***et al.*** **Lower ferroelectric coercive field of ScGaN with equivalent remanent polarization as ScAlN.** ***Applied Physics Express*** **15, 081003 (2022).**
11. **Fichtner, S., Wolff, N., Lofink, F., Kienle, L. & Wagner, B. AlScN: A III-V semiconductor based ferroelectric.** ***J. Appl. Phys.*** **125, (2019).**
12. **Balestra, L., Gnani, E. & Reggiani, S. Electron effective masses of Sc** ***x*** **Al1− *x* N and Al *x* Ga1− *x* N from first-principles calculations of unfolded band structure.** ***J. Appl. Phys.*** **132, (2022).**
13. **Furuta, K.** ***et al.*** **First-principles calculations of spontaneous polarization in ScAlN.** ***J. Appl. Phys.*** **130, (2021).**
14. **Ludt, C., Meyer, D. C. & Zschornak, M. Ferroelectric Phase Transition in Barium Titanate Revisited with Ab Initio Molecular Dynamics.** ***Materials*** **17, 1023 (2024).**
15. **Tan, Z., Peng, Y., An, J., Zhang, Q. & Zhu, J. Critical Role of Order–Disorder Behavior in Perovskite Ferroelectric KNbO $_{3}$.** ***Inorg. Chem.*** **60, 7961–7973 (2021).**
16. **Koyama, T., Yokoyama, Y., Tanibata, N., Takeda, H. & Nakayama, M. Efficient optimization of atom/ion arrangements in crystalline solids**

using genetic algorithms and machine-learning regression. *Journal of the Ceramic Society of Japan* 133, 25006 (2025).
17. Zhu, Q., Xie, Y., Xuan, W., Xu, S. & Ren, Z. Prediction of cross-material properties of mineralized ceramic core of aluminosilicate system based on deep learning. *Journal of the Ceramic Society of Japan* 133, 24107 (2025).
18. Mizoguchi, T. A review of simulation, characterization, and informatics in inorganic materials. *Journal of the Ceramic Society of Japan* 133, 25121 (2025).
19. Chen, P.-Y., Shibata, K., Hagita, K., Miyata, T. & Mizoguchi, T. Prediction of the Ground-State Electronic Structure from Core-Loss Spectra of Organic Molecules by Machine Learning. *J. Phys. Chem. Lett.* 14, 4858–4865 (2023).
20. Meng, H., Liu, Y., Yu, H., Zhuang, L. & Chu, Y. Machine-learning-potential-driven prediction of high-entropy ceramics with ultra-high melting points. *Cell Rep. Phys. Sci.* 6, 102449 (2025).
21. Zhang, J. *et al.* Vacancy-induced phonon localization in boron arsenide using a unified neural network interatomic potential. *Cell Rep. Phys. Sci.* 5, 101760 (2024).
22. Li, Q.-J. *et al.* Development of robust neural-network interatomic potential for molten salt. *Cell Rep. Phys. Sci.* 2, 100359 (2021).
23. Chen, P.-Y., Shibata, K. & Mizoguchi, T. High precision machine learning force field development for BaTiO3 phase transitions, amorphous, and liquid structures. *APL Machine Learning* 3, (2025).
24. Chen, P. & Mizoguchi, T. Effect of uniaxial compressive stress on polarization switching and domain wall formation in tetragonal phase BaTiO3 via machine learning potential. *Mater. Des.* 265, 115851 (2026).
25. Chen, P.-Y. & Mizoguchi, T. Electric Field-Induced Phase Transitions and Hysteresis in Ferroelectric HfO2 Captured with Machine Learning Potential. arXiv:2511.09976, (2025).
26. Batatia, I. *et al.* A foundation model for atomistic materials chemistry. arXiv:2401.00096, (2025).
27. Kutana, A., Shimizu, K., Watanabe, S. & Asahi, R. Representing Born effective charges with equivariant graph convolutional neural networks. *Sci. Rep.* 15, 16719 (2025).
28. Ji, Y., Liang, J. & Xu, Z. Machine-Learning Interatomic Potentials for Long-Range Systems. *Phys. Rev. Lett.* 135, 178001 (2025).
29. Yasuoka, S. *et al.* Effects of deposition conditions on the ferroelectric properties of (Al1− x Sc x)N thin films. *J. Appl. Phys.* 128, (2020).
30. Schönweger, G. *et al.* From Fully Strained to Relaxed: Epitaxial Ferroelectric Al $_{1-x}$ Sc $_{x}$ N for III-N Technology. *Adv. Funct. Mater.* 32, (2022).
31. Wang, P. *et al.* Fully epitaxial ferroelectric ScAlN grown by molecular beam epitaxy. *Appl. Phys. Lett.* 118, (2021).
32. Wang, P., Wang, D., Mondal, S. & Mi, Z. Ferroelectric N-polar ScAlN/GaN heterostructures grown by molecular beam epitaxy. *Appl. Phys. Lett.* 121, (2022).
33. Wolff, N. *et al.* Demonstration and STEM Analysis of Ferroelectric Switching in MOCVD-Grown Single Crystalline Al $_{0.85}$ Sc $_{0.15}$ N. *Advanced Physics Research* 3, (2024).

34. **Dong, H. *et al.* Thermal transport in disordered wurtzite ScAlN alloys using machine learning interatomic potentials. *Mater. Today Commun.* 39, 109213 (2024).**
35. **Kresse, G. & Hafner, J. *Ab initio* molecular dynamics for liquid metals. *Phys. Rev. B* 47, 558–561 (1993).**
36. **Kresse, G. & Furthmüller, J. Efficient iterative schemes for *ab initio* total-energy calculations using a plane-wave basis set. *Phys. Rev. B* 54, 11169–11186 (1996).**
37. **Kresse, G. & Hafner, J. *Ab initio* molecular-dynamics simulation of the liquid-metal–amorphous-semiconductor transition in germanium. *Phys. Rev. B* 49, 14251–14269 (1994).**
38. **Kresse, G. & Furthmüller, J. Efficiency of ab-initio total energy calculations for metals and semiconductors using a plane-wave basis set. *Comput. Mater. Sci.* 6, 15–50 (1996).**
39. **Blöchl, P. E. Projector augmented-wave method. *Phys. Rev. B* 50, 17953–17979 (1994).**
40. **Perdew, J. P., Burke, K. & Ernzerhof, M. Generalized Gradient Approximation Made Simple. *Phys. Rev. Lett.* 77, 3865–3868 (1996).**
41. **Maintz, S., Deringer, V. L., Tchougréeff, A. L. & Dronskowski, R. Analytic projection from plane-wave and PAW wavefunctions and application to chemical-bonding analysis in solids. *J. Comput. Chem.* 34, 2557–2567 (2013).**
42. **Maintz, S., Deringer, V. L., Tchougréeff, A. L. & Dronskowski, R. LOBSTER: A tool to extract chemical bonding from plane-wave based DFT. *J. Comput. Chem.* 37, 1030–1035 (2016).**
43. **Nelson, R. *et al.* <scp>LOBSTER</scp> : Local orbital projections, atomic charges, and chemical-bonding analysis from <scp>projector-augmented-wave-based</scp> density-functional theory. *J. Comput. Chem.* 41, 1931–1940 (2020).**
44. **Lichtensteiger, C. *et al.* Ferroelectricity in ultrathin film capacitors. arXiv:1208.5309, (2012).**
45. **Ghosez, Ph., Michenaud, J.-P. & Gonze, X. Dynamical atomic charges: The case of <math display="inline"> <mi>AB</mi> <mrow> <msub> <mrow> <mi mathvariant="normal">O</mi> </mrow> <mrow> <mn>3</mn> </mrow> </msub> </mrow> </math> compounds. *Phys. Rev. B* 58, 6224–6240 (1998).**
46. **Shimizu, K., Otsuka, R., Hara, M., Minamitani, E. & Watanabe, S. Prediction of Born effective charges using neural network to study ion migration under electric fields: applications to crystalline and amorphous Li_3PO_4. *Science and Technology of Advanced Materials: Methods* 3, (2023).**

Supplementary Files

This is a list of supplementary files associated with this preprint. Click to download.

- RSahashietalScAlN1SI.docx
- RSahashietalScAlN1MovieS.mp4